

Supplementary Materials for Asymmetric photoelectric effect: Auger-assisted hot hole photocurrents in transition metal dichalcogenides

Andrey Sushko,^{1,*} Kristiaan De Greve,^{1,2,3} Madeleine Phillips,⁴ Bernhard Urbaszek,⁵
Andrew Y. Joe,¹ Kenji Watanabe,⁶ Takashi Taniguchi,⁷ Alexander L. Efros,⁴
C. Stephen Hellberg,⁴ Hongkun Park,^{1,2} Philip Kim,¹ and Mikhail D. Lukin¹

¹*Department of Physics, Harvard University,
Cambridge, Massachusetts 02138, USA*

²*Department of Chemistry and Chemical Biology,
Harvard University, Cambridge, Massachusetts 02138, USA*

³*Currently at Imec, Kapeldreef 75, Leuven, Belgium*

⁴*Naval Research Laboratory (NRL), Washington, DC, 20375*

⁵*Université de Toulouse, INSA-CNRS-UPS, LPCNO,
135 Avenue Rangueil, 31077 Toulouse, France*

⁶*Research Center for Functional Materials,
, National Institute for Materials Science,
1-1 Namiki, Tsukuba, 305-0044, Japan*

⁷*International Center for Materials Nanoarchitectonics,
National Institute for Materials Science,
1-1 Namiki, Tsukuba, 305-0044, Japan*

(Dated: September 22, 2020)

* asushko@g.harvard.edu

I. EXPERIMENTAL METHODS

Transport and optical characterisation is performed at 6 K in a closed cycle cryostat with optical access via a free-space confocal system with a 0.75 NA objective. For many experiments, two individually steerable beam paths are used to concurrently excite different regions of the nanofabricated device structures at independently varying intensity and wavelength. A temperature-stabilised CW 660nm laser diode is employed for off-resonant excitation, while wavelength dependent studies are performed with a tunable CW Ti:sapphire laser source. Unless explicitly stated otherwise, all measurements are performed with contacts to the TMD at 0 V for ease of interpretation of local gate voltage. Heterostructures are assembled from exfoliated flakes using a dry-transfer technique with a PC-PDMS polymer stamp, deposited on Si/285 nm SiO₂ chips, and characterised with AFM to determine layer thicknesses. Twist angle between the hBN and TMD layers is random in all devices. Contacts and metal gates, where present, are patterned using electron-beam lithography followed by thermal evaporation. Numerous devices are employed in this work, with their key structural properties provided in Table 1.

II. DFT METHODS

We carry out density functional theory (DFT) calculations in VASP [1] using hybrid functionals (HSE06 [2]). For the hBN layer, we use boron potentials with 3 valence electrons and nitrogen potentials with 5 valence electrons. For the transition metal dichalcogenide (TMD) layer, we use metal potentials with 14 valence electrons and selenium potentials with 6 valence electrons. Van der waals forces between layers are accounted for using the DFT-D3 method of Grimme [3]. Individual monolayers were relaxed with a 6x6x1 Γ -centered k-point mesh at a variety of in-plane lattice constants to obtain the following optimized monolayer lattice constants: $a_{hBN} = 2.492\text{\AA}$, $a_{MoSe_2} = 3.26\text{\AA}$, $a_{WSe_2} = 3.252\text{\AA}$. We construct bilayers with a supercell consisting of 7 TMD unit cells on top of 12 hBN unit cells, with the hBN strained to match the TMD layer. In the MoSe₂/hBN bilayer, the hBN is compressively strained by 0.09%, and in the WSe₂/hBN bilayer, the hBN is compressively strained by 0.33%. In both systems, the layers are twisted with a 10.89° angle between them. The density of states is computed with spin-orbit coupling on a 12x12x1 Γ -centered k-point

mesh. In all cases, the out-of-plane lattice constant is 30\AA , resulting in approximately 23\AA of vacuum in each case. To construct the smooth density of states plots in Figure 4a, b, each state is given a gaussian profile in energy with standard deviation $\sigma = 0.08$, and we use energy bins of width 10 meV. The hybridization of a given state is determined by extracting the fraction of the wavefunction localized in the TMD layer (x) and plugging it into a parabolic function $h(x) = -4x(x - 1)$, where $x \in [0, 1]$. Doping was not accounted for in our first-principles calculations. Because the experiments showed that the exciton and trion energies did not vary significantly with doping, we judged that band renormalization due to doping does not play a major role in the physics of the hBN/TMD interface (though it does affect exciton generation under narrow on-resonant excitation as in Fig S10). Furthermore, we use the DFT calculations qualitatively rather than quantitatively in this study. All quantitative estimates come from the kinetic model and the Fowler-Nordheim model fitting the experimental data.

The 10.89° twisted supercell was chosen not because of any significance of this angle, but to minimize strain in the first-principles calculations while still being small enough to avoid excessive computational expense. The relative twist angle between hBN and TMD was not controlled during the experimental fabrication process, so samples likely exist at a variety of angles, and all exhibit the same photocurrent behavior. This is consistent with our DFT calculations: in addition to the 10.89° calculations, we also computed the layer-hybridized density of states for hBN/MoSe₂ and hBN/WSe₂ bilayers with a relative rotation angle of 19.1° , and the results are qualitatively the same. There are more hybridized states available to holes excited by a h^+-X^0 Auger process in the MoSe₂ system than in the WSe₂ system (See Fig. S1). There are differences in band energies computed with DFT for the two different angles, but these likely arise from the different amounts of strain in the computation supercells. This strain is introduced to make the computations tractable and likely would not be present to a comparable extent in the real heterostructure.

To see that the strain does not significantly affect band morphology in the bilayers, we show in Fig. S2 the bands for the 19.1° bilayers with the hBN strained/TMD unstrained (a,b), and then with the hBN unstrained/TMD strained (c,d). While the band energies are somewhat altered with strain, the band morphologies remain very similar.

III. KINETIC MODEL AND DOPING-DEPENDENT QE FITS

To better understand the photocurrent in these systems, we derive an expression for the photocurrent (quantum efficiency) from a set of kinetic equations that describes particles in the TMD layer. We first write the expression for the neutral excitons (n_X) in the TMD:

$$\frac{\partial n_X}{\partial t} = g_{eh} - \frac{n_X}{\tau} - \frac{1}{\tau_A^B} n_X^2 - h_g \frac{n_X}{\tau_A^T} \quad (1)$$

where g_{eh} is the electron-hole generation rate, which is proportional to the laser power. τ^{-1} is a time constant describing the radiative and non-radiative (but not Auger) recombination of excitons: $\tau^{-1} = \tau_r^{-1} + \tau_{nr}^{-1}$. h_g is the number of ground state holes, τ_A^T is the time constant describing Auger recombination of excitons, and τ_A^B is the time constant for exciton-exciton annihilation. Our experiments are carried out in the low-pumping regime, as shown by measurements of current that are linear in laser power (Fig 2c), and in this regime, we can ignore the quadratic n_X term. We assume the low-pumping limit in all the equations that follow. If we also work in the steady state limit, we obtain $n_X = g_{eh}\tau_d$, where $1/\tau_d = 1/\tau + h_g/\tau_A^T$.

The equation describing the excited holes, h_e is as follows:

$$\frac{\partial h_e}{\partial t} = h_g \frac{n_X}{\tau_A^T} - \frac{h_e}{\tau_{tun}} - \frac{h_e}{\tau_{ter}} \quad (2)$$

where τ_{ter} is the time it takes an excited hole to thermalize, and τ_{tun} is the time it takes an excited hole to tunnel into the hBN. Finally, the expression for the ground state holes in the system is

$$\frac{\partial h_g}{\partial t} = \frac{h_e}{\tau_{ter}} - h_g \frac{n_X}{\tau_A^T} + \frac{h_e}{\tau_{tun}} \quad (3)$$

The h_e/τ_{tun} term represents the current of ground state holes flowing into the TMD layer. It exactly balances the expression for excited holes tunneling out of the TMD because we assume we are operating in steady state. If we solve equation (3) in the steady state, we obtain the expression $h_e = h_g n_X \tau_{ex}/\tau_A^T$, where $1/\tau_{ex} = 1/\tau_{ter} + 1/\tau_{tun}$.

Since we are interested in the photocurrent, we write an expression for the quantum efficiency (QE), which is roughly the current divided by laser power:

$$QE = \frac{h_e}{\tau_{tun} g_{eh}} \quad (4)$$

and using our expressions for n_X in the steady state, low-pumping limit and h_e in the steady state limit, we obtain the following expression:

$$QE = \frac{h_g}{(\tau_{tun}/\tau_{ter} + 1)(\tau_A^T/\tau + h_g)} \quad (5)$$

This expression for quantum efficiency is dependent only on the hole-doping in the TMD, so we can use it to fit measurements of photocurrent as a function of doping. These fits are shown in Figs. 4c,d of the main text, along with the extracted approximate values of τ_{tun}/τ_{ter} and τ_A^T/τ for each system. While the expression in Equation (5) doesn't account for all the features in the QE data, it does capture an important difference between WSe₂ and MoSe₂: the ratio τ_A^T/τ is the same order of magnitude in the two systems, but the ratio τ_{tun}/τ_{ter} is two orders of magnitude larger in the WSe₂ system as in the MoSe₂ system. Thermalization of excited holes is more efficient than tunneling in both systems, but in the WSe₂ system, thermalization is *much* more efficient, which is consistent with the larger amounts of photocurrent measured in the MoSe₂ system.

IV. DUAL-GATE PHOTOCURRENT COMPETITION

Figure S3 expands on the dual-gate current dependence data from Fig. 2 of the main text, showing the currents to the top gate, bottom gate, and their sum independently. The behaviour of the bottom gate is completely analogous to the top. The total current, however, highlights that the decrease in current observed when both gates are negative can be attributed to a limited supply of hot holes tunneling in two competing directions thus reducing the current to either gate while maintaining the total.

V. DISSOCIATION DOPING POWER DEPENDENCE

Several other experiments were conducted to evaluate the impact of photodoping in MoSe₂ devices. In Fig S4, we consider the dependence of the spatial map of photocurrent on the power of the confocally scanned excitation laser. We note that at increasing power, appreciable photocurrent is only observed while the gate edges are illuminated, indicating

that photodoping is the dominant doping mechanism at high optical power. At very low power (Fig. S4c) we see roughly uniform current from the entire device area, suggesting that a weak hole doping mechanism exists to replenish holes in the absence of photodoping.

We explore the relative efficiencies of photocurrent and photodoping in Fig. S5 by considering the dependence of photocurrent and trion PL emission on two laser powers. An excitation spot is placed in the center of the device to generate photocurrent, with the same optical path used to collect PL. A second laser is focused on a gate edge to provide holes via dissociation doping. Varying the power of the two lasers demonstrates comparable process efficiencies. The discrepancy between photocurrent and PL at low excitation spot power is attributed to the fact that the doping laser is also able to partially excite photocurrent from the part of the optical spot that overlaps the gated region, while the PL collection occurs only at the center.

Figure S6 explores a similar effect to Fig. S4 on a MoSe₂ device with 90 nm thick hBN and a thin metal bottom gate outlined in both panels. Scanning a single excitation spot over a local gate biased to -8 V produces edge-dominated photocurrent as in Fig. S4e due to the need for photodoping. However, placing a considerably stronger fixed laser at the gate edge and scanning a weak excitation laser, gives rise to a uniform photocurrent increase when illuminating the gated region, indicating that an adequate supply of holes is being provided by the edge excitation. It is important to note that the QE numbers consider only the photocurrent difference produced by the scanning laser, after subtracting the substantially higher constant photocurrent due to the edge excitation laser's overlap with the gated area and resulting photocurrent generation.

VI. PHOTOCURRENT AND UPCONVERSION

In Fig. S7a, we consider upconverted PL from resonant excitation of a MoSe₂ device, compared to the white light reflectance (Fig. S7b). As in Fig. 5 of the main text, we see that while the Lower energy s2 Rydberg state of the A exciton is suppressed by hole doping, the B exciton persists in the doped regime, while upconverted PL emission drops off rapidly with hole or electron doping. Photocurrent onset (Fig. S7c) corresponds similarly to the dropoff in upconverted PL. In these data, we also clearly see symmetric behaviour on the electron side in PL and reflectance, suggesting competition with hot electron generation.

Due to the comparatively higher barrier, however, these electrons are not able to tunnel through the hBN leading to asymmetry in the photocurrent data.

VII. PHOTOCURRENT SPATIAL UNIFORMITY

By confocally scanning the excitation laser over a sample, we investigate the spatial uniformity of the photocurrent process. In Fig S4, we provide a discussion demonstrating the current is spatially uniform over an electrode when sufficient hole-doping is provided to the MoSe₂ by dissociation. Similarly, Fig. S4c shows increasingly uniform current at low excitation power when inefficient hole-doping mechanisms can maintain the doping of the material. In WSe₂, meanwhile, hole-doping can be achieved efficiently via the edge contacts allowing us to examine the spatial distribution in the simplest configuration, using a single scanned excitation laser of arbitrary intensity. The results of this experiment are presented in Fig. S8 for a WSe₂ monolayer separated by 12 nm hBN from a graphite bottom gate (device F). Comparing the map of photocurrent generation (Fig. S8b), we see a higher degree of uniformity than the PL emission (Fig. S8c), suggesting that the uniformity in this device is limited by material cleanliness rather than intrinsic properties of the process. Taken together, these varied experiments support the model of a photocurrent process that is intrinsic to the TMD-hBN system and not mediated by particular defects or electric field configuration.

VIII. MOSE₂ CONTACT VERIFICATION

To evaluate the performance of edge contacts on an MoSe₂ device at the 6 K operating temperature, we consider experiments on device C, which was fabricated with contacts on both sides of a locally bottom-gated region, as shown in Fig. S9a. To activate the contacts, we excite with a pair of confocal 50 μ W 660nm lasers at the interface between the metal and TMD. The excitation occurs far enough from the gated region so as to not induce any significant photocurrent, but allows the contacts to source and sink a substantial current relatively symmetrically. In Fig. S9b, we plot the source-drain current between the two contacts while driving one in opposition to the other, for varying values of local gate bias in the center region of the device. These curves are consistent with electron current through the

contacts, with a flat band condition at approximately 0.25 V bottom gate voltage. For positive gate bias, the curves are limited by the source-drain voltage difference while for negative bias it presents a barrier to source-drain current. Plotting the current as a 2-dimensional function of contact voltage and gate voltage shows a unity slope to the onset of current - a result that is consistent with n-type carriers. Finally, we observe that the optical excitation applied to the contacts only impacts the current for the contact that sources electrons and is not necessary on the contact that accepts electrons. This behaviour aligns well with photocurrent measurements in which exciton dissociation is able to hole dope part of the device by generating an electron-current into one of the contacts and a corresponding hole current into the gated region. Those accumulated holes can subsequently be photoexcited through the hBN, with the contact resistance not significantly rate limiting for the optical powers used in these studies. This conclusion is reinforced by the linear dependence of the photocurrent processes on optical power, indicating that increasing photocurrent does not substantially alter the electrostatic conditions in the experiments used to examine Auger process efficiency.

Resonant excitation can give further insight on the doping conditions in MoSe₂. Due to the shift of the exciton resonance with doping, photocurrent at fixed excitation wavelength can be seen to peak at a particular doping as shown in Fig. S10. When photocurrent rate approaches the rate of dissociation doping a shift is observed corresponding to a change in doping conditions vs gate voltage due to inadequate hole replenishment rate. For MoSe₂ data discussed in the main text, care is taken to verify that no significant shift is observed with varying optical power such that the results are not confounded by inadequate hole replenishment.

IX. RESONANT EXCITATION EFFICIENCY COMPARISON

Due to the expected differences in off-resonant (660 nm) excitation efficiency we consider resonant excitation of both materials in Fig S11. While the efficiency of WSe₂ is higher under resonant excitation, as might be expected, that difference accounts for only a small part of the total disparity between the two materials. As laid out in the main text, we ascribe the remaining difference to the distinct valence band alignments between the TMD and hBN.

X. CONTACTLESS HOLE INJECTION AND GATE-DRAGGING EFFECTS

In contrast to the other devices in this study, where optical excitation was performed in a region with a conductive local gate opposite the TMD, we consider here a phenomenon that occurs when an hBN-encapsulated TMD structure is placed directly over an Si/SiO₂ wafer bottom gate. In this structure, gating through the combined 285 nm SiO₂/50 nm hBN can achieve doping control similarly to locally gated structures. Hot holes, however, can only cross the hBN layer and are stopped by the oxide leading to no measurable photocurrent. We do, however, observe an indication of the process via hysteretic doping behaviour of the TMD as the Si bottom gate is varied. When swept from an electron doped regime at positive gate voltage towards negative voltage, PL measurements indicate a transition through charge neutrality and towards mild hole doping but do not indicate any greater doping for increasingly negative gate voltage. Reversing the sweep towards positive, however, quickly brings the device through to electron doping much earlier than would be expected from the downward sweep. An example of this effect is provided in Fig. S12. Furthermore, after repeated sweeps to increasingly negative voltage, the transition towards electron doping on the upward sweep and away from electron doping on the subsequent down sweep will also shift down to a voltage slightly above that at which the previous sweep turned around. This “ratcheting” behaviour and inability to significantly hole dope is consistent with photocurrent across the hBN establishing a layer of positive charge at the hBN-SiO₂ interface, screening the bottom gate thus preventing further doping. Due to the lack of electrical contact to this interface, the positive charge persists upon increased bottom gate voltage, substantially shifting the condition for charge neutrality. This charging was observed to dissipate over the course of multiple hours, gradually restoring the initial charge neutrality conditions for the device.

XI. TABLE 1: DEVICE STRUCTURES

Below is a table of the properties of all device structures used in this manuscript. Photocurrent was also observed in numerous other similar devices that are not discussed due to redundancy.

Device	TMD	Top hBN	Bottom hBN	Contacts	Top gate	Bottom gate
A	MoSe ₂	55 nm	90 nm	Pt	-	6 nm Au
B	MoSe ₂ /WSe ₂	60 nm	50 nm	Pt	6 nm Au	6 nm Au
C	MoSe ₂	27 nm	3 nm	Cr/Au	-	3 nm graphite
D	WSe ₂	50 nm	70 nm	Pt	-	6 nm Au
E	MoSe ₂	O(50 nm)	O(50 nm)	Pt	-	Si/285 nm SiO ₂
F	WSe ₂	O(40 nm)	12 nm	Pt	-	3 nm graphite

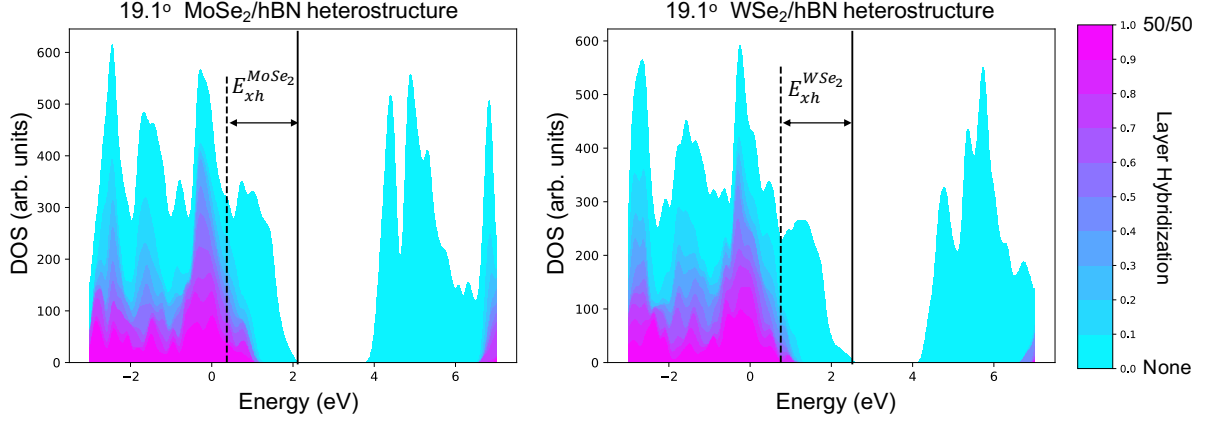


FIG. 1. | **Hybridized Density of States (DOS) for 19.1° twisted supercell** The 19.1° twisted supercell contains 4 unit cells of TMD and 7 unit cells of hBN. In these calculations, the TMD is left unstrained and the hBN layer is compressively strained by 1.1% for the MoSe₂ system and by 1.4% for the WSe₂ system. All other calculation parameters are the same as those listed for the 10.89° twisted supercell. In agreement with the experiments, which show that the photocurrent behavior persists across samples with uncontrolled twist angles, the relative differences in DOS between the two systems shown here are qualitatively the same as the differences between the MoSe₂ and WSe₂ systems in the 10.89° supercell.

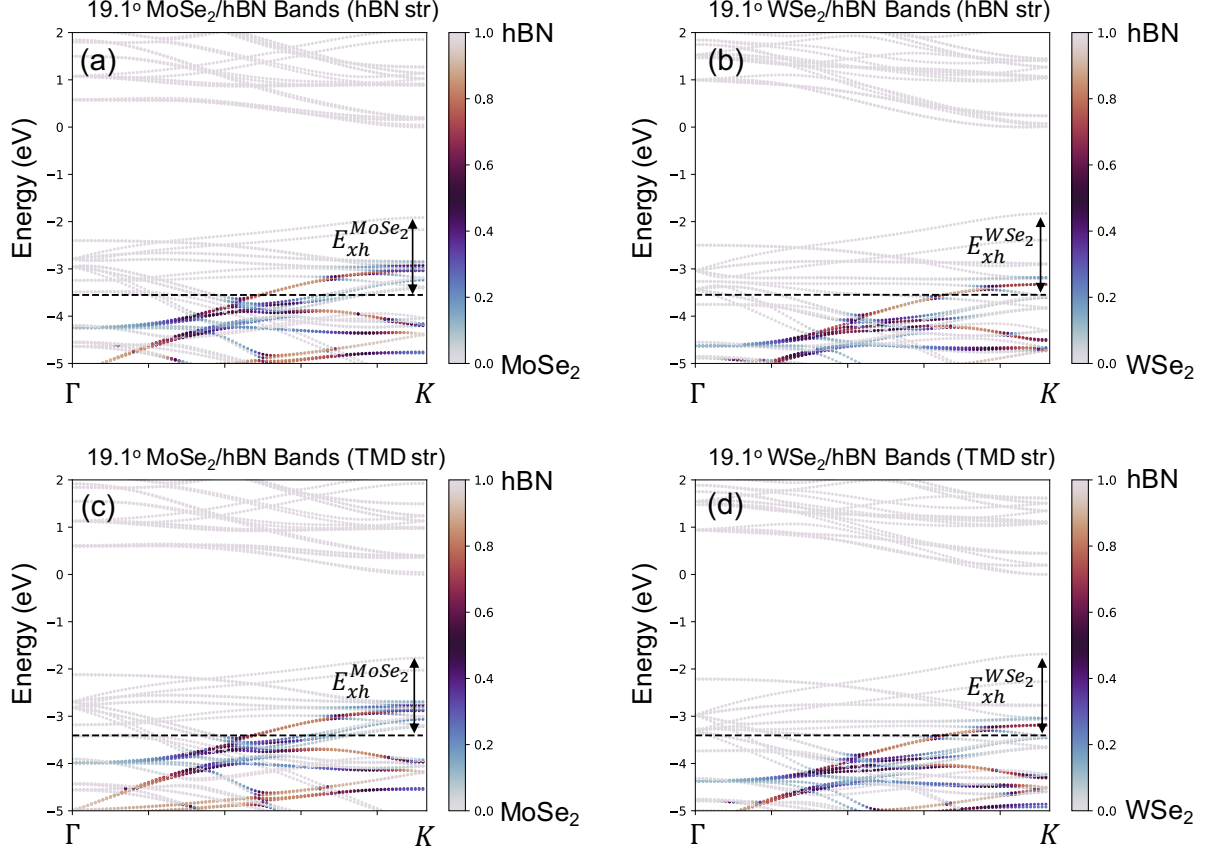


FIG. 2. | **Effect of strain on band structures for 19.1° twisted supercell** Band structures for TMD/hBN bilayers with a 19.1° twist with **a,b)** the hBN layer compressively strained by 1.1% and 1.4%, respectively and **c,d)** the TMD layer under tensile strain of 1.1% and 1.4%, respectively. Although the band energies change noticeably with strain, the change in band morphologies with strain is minimal. Dashed lines mark the neutral exciton energy measured from the valence band maximum. Layer-polarized bands are colored light gray, while bands of any other color are layer-hybridized to the degree indicated by the color bar.

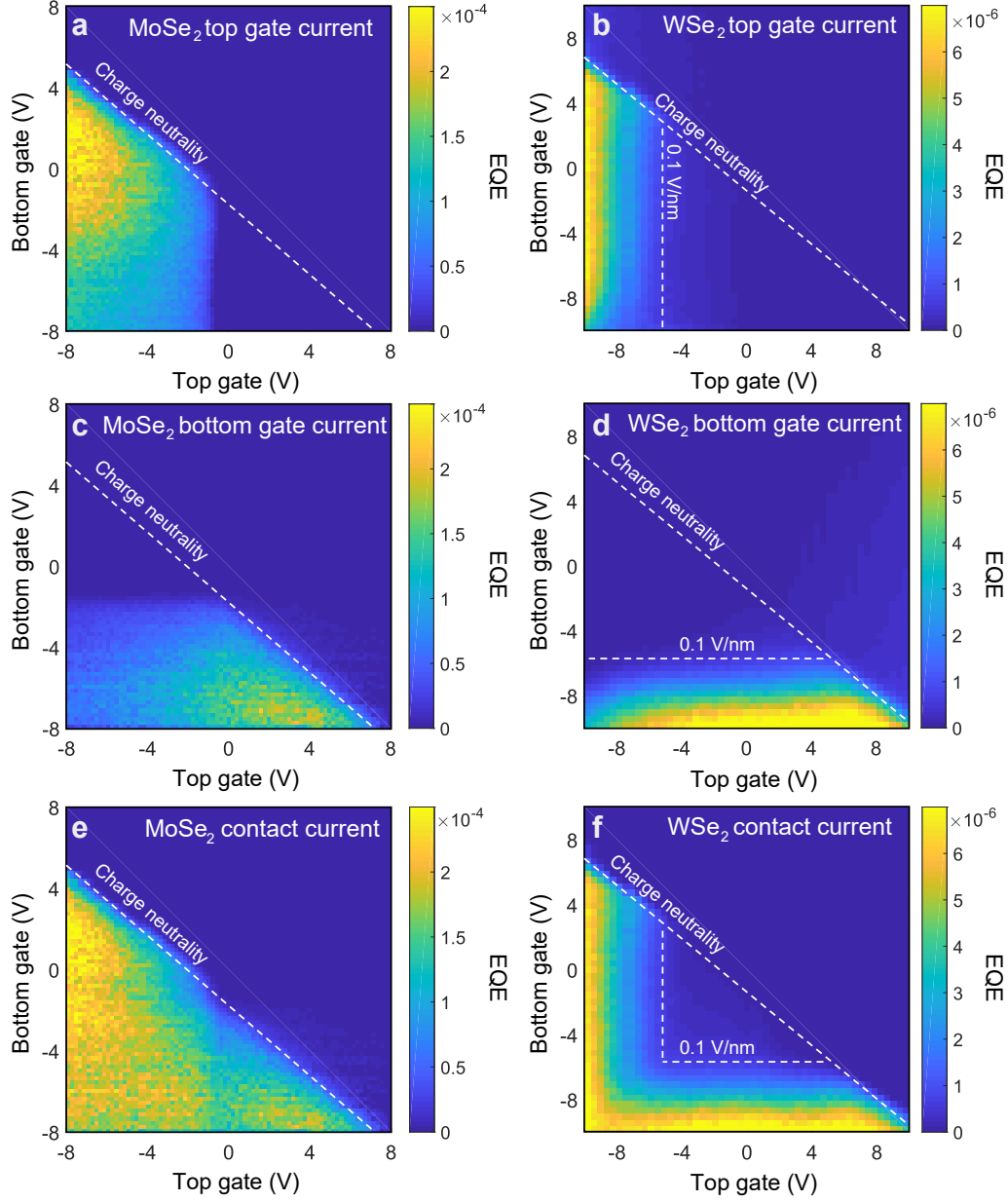


FIG. 3. | **Dual-gate photocurrent measurement** **a,b)** Top gate currents for MoSe₂ and WSe₂ reproduced from Fig. 2 of the main text, shown alongside the bottom gate currents (**c,d**) and contact currents (computed here as the sum of the two gate currents) (**e,f**). We note that current only occurs under both hole doping and field that draws holes towards the relevant gate. In the case of WSe₂, the required field is significantly larger resulting in minimal current for the region of field with magnitude below 0.1 V/nm marked in (**f**). The reduction in individual top and bottom gate current when both gates are negative does not correspond to a reduction in the total photocurrent, indicating that the two gates compete for available hot holes.

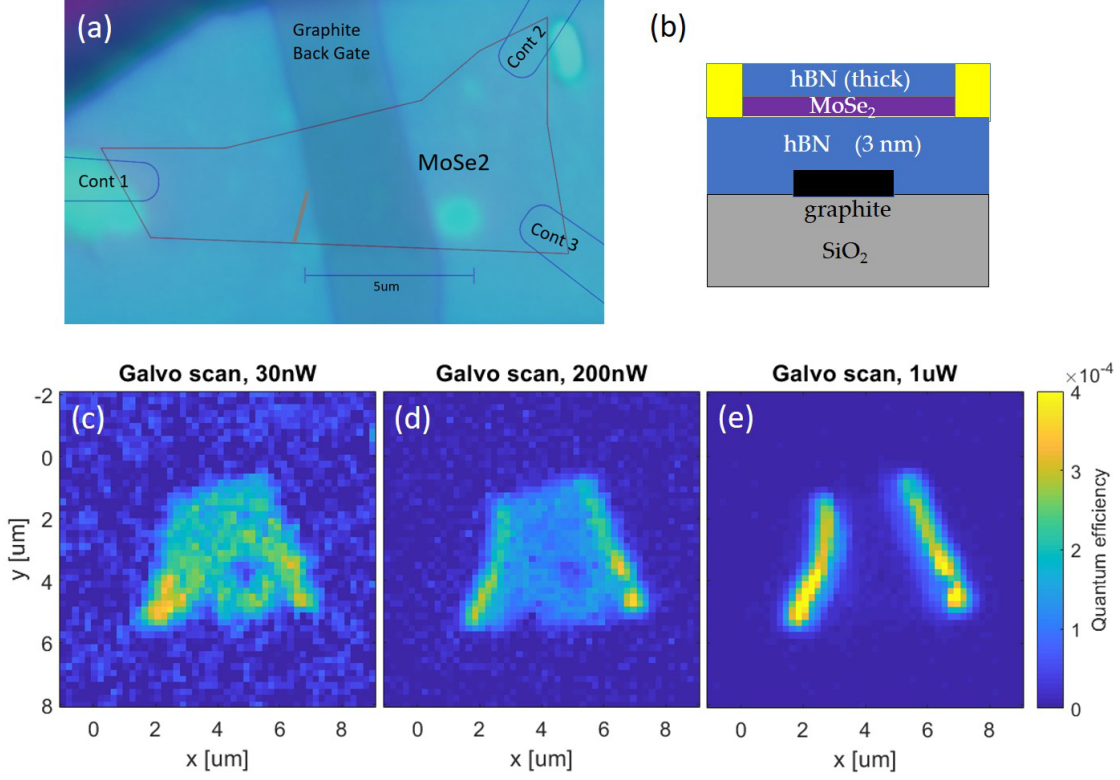


FIG. 4. | **Spatially resolved dissociation doping via photocurrent** a) Annotated microscope image of an encapsulated MoSe₂ device with schematic in (b). c,d,e) Maps of photocurrent under scanning of optical excitation at varying power. Under increasing power, the inability of contacts to source holes restricts photocurrent generation to the edges of the gated region where lateral fields allow for doping via dissociation of excitons.

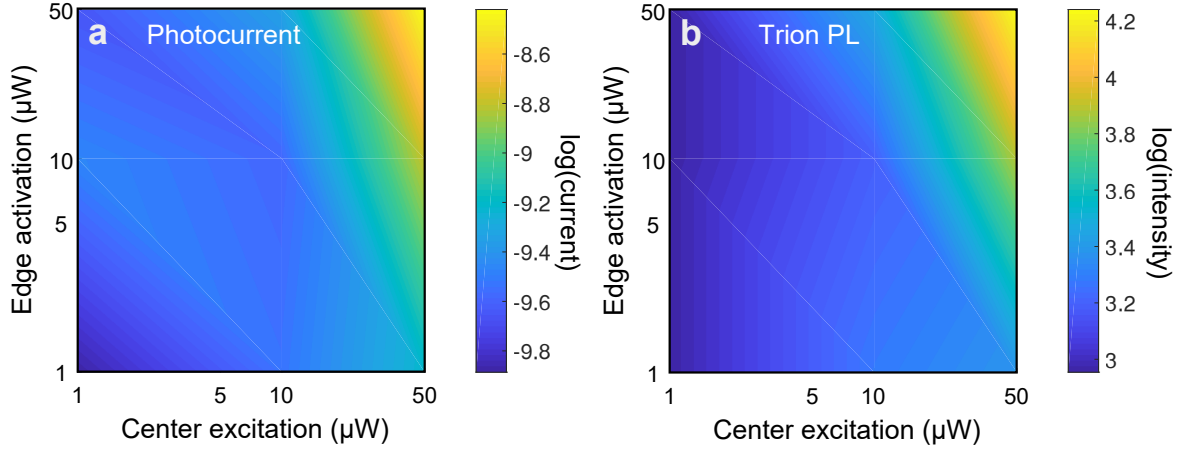


FIG. 5. | **Dependence on excitation and photodoping power** a) Photocurrent and b) trion PL as a function of the optical power at a fixed excitation spot in the center of the device in Fig. S4 and a fixed photodoping spot at a gate edge.

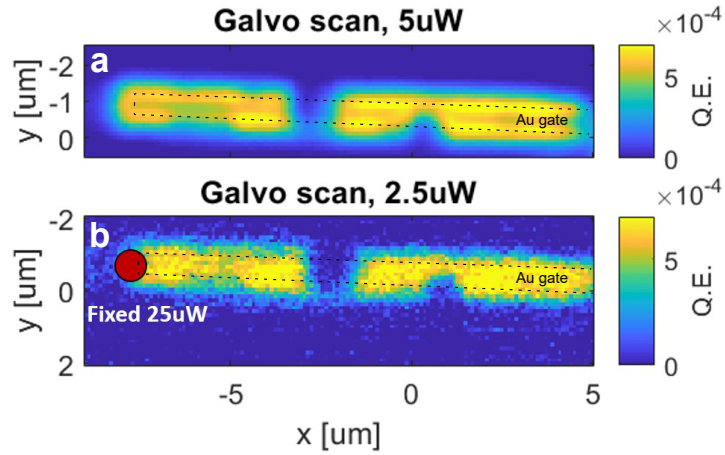


FIG. 6. | **Spatially resolved dissociation doping via photocurrent** Spatial maps of photocurrent under scanned single point 5 μW 660 nm excitation (a) and, in (b), strong fixed edge excitation (25 μW 660 nm) accompanied by weak scanned excitation (2.5 μW 660 nm). Quantum efficiency figures are computed subtracting away the current due to fixed excitation.

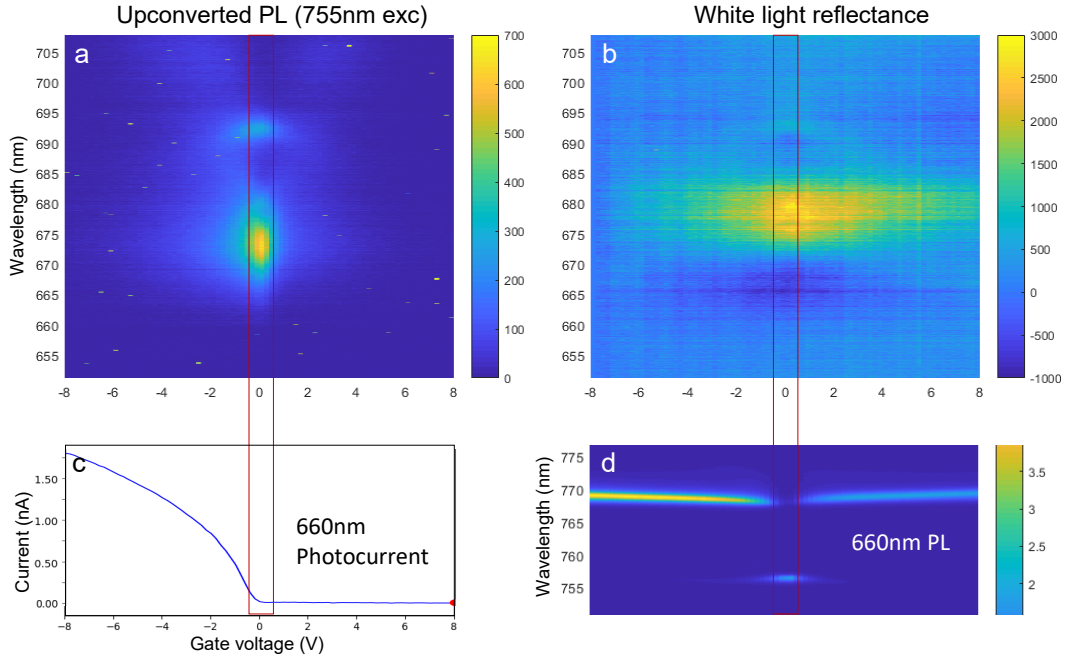


FIG. 7. | **Photocurrent competition with exciton upconversion** Analogous data to Fig. 5 of the main text, demonstrated on a MoSe₂ device with 90 nm thick hBN rather than 3 nm. Despite the substantial difference in thickness, the devices exhibit equivalent physics as would be expected for the proposed Auger model.

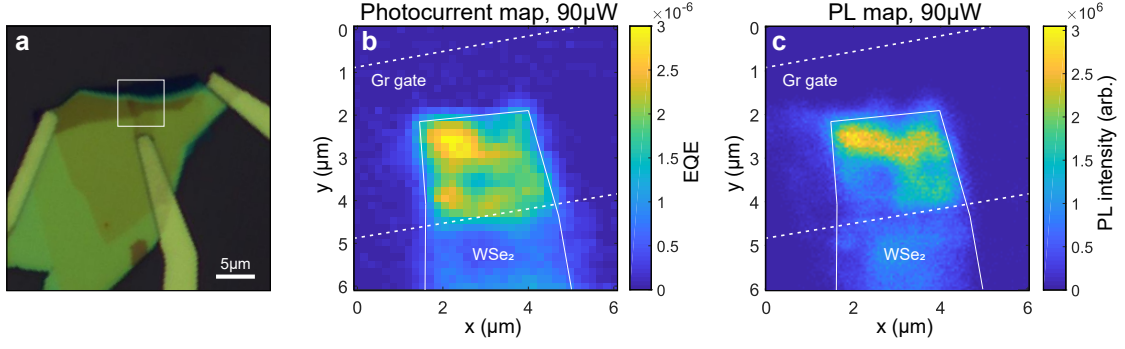


FIG. 8. | **WSe₂ photocurrent spatial mapping** **a)** Optical image of a WSe₂ monolayer device separated from a graphite bottom gate by 12nm hBN. **b, c)** Photocurrent and PL maps over the device region indicated by the white square in (a), respectively. Photocurrent is present over the WSe₂ region located over the bottom gate, showing greater spatial uniformity than the PL data.

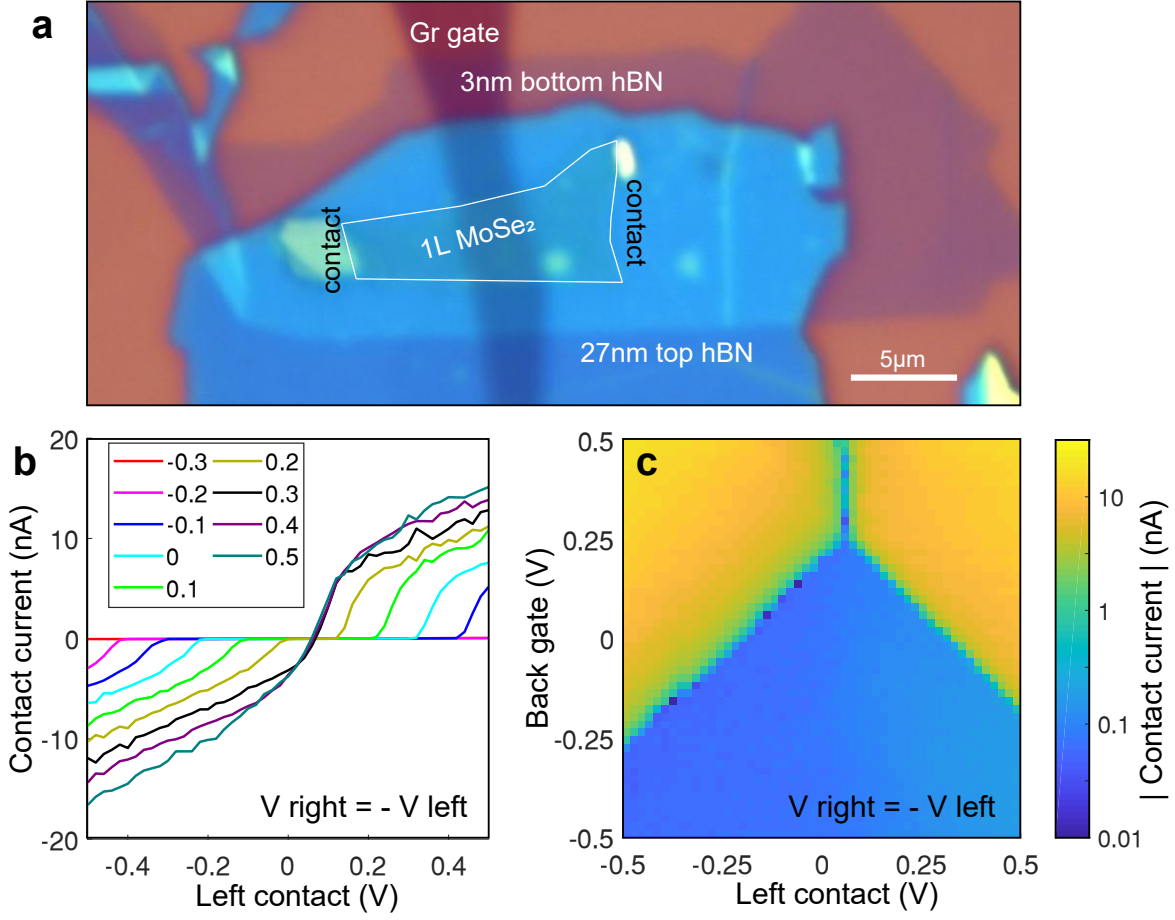


FIG. 9. | **MoSe₂ contact verification** **a)** Optical image of device C (MoSe₂ monolayer, 3nm hBN) prior to contact fabrication, highlighting the device structure and location of subsequently fabricated edge contacts to the MoSe₂. **b, c)** Current at the left contact when driving the two contacts in opposition to each other while varying the voltage on the graphite bottom gate. Measurements are performed at 6 K. Optical excitation is applied at the contacts, far away from the gated region such that no significant photocurrent to the bottom gate is observed. The data are consistent with an electron current across a pair of junctions generated by the potential step at the gate edges, with flat-band conditions at approximately 0.25 V on the gate. We note the ability of these contacts to source significant electron-current, in excess of 5 nA at a source-drain bias of 0.1 V.

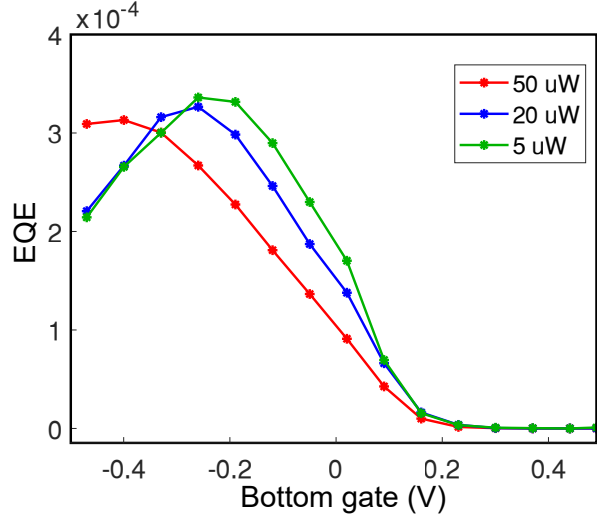


FIG. 10. | **Signatures of inadequate hole replenishment** Data taken from a bottom gated MoSe₂ device (device C) with 50 μ W 660 nm excitation at the gate edge for dissociation doping, and exciton-resonant 757 nm excitation of varying power over the gated region. Due to the shift in resonance with doping, the EQE peaks at a certain doping level. For increasing center excitation power, the photocurrent generation exceeds the rate of hole-doping via dissociation, resulting in lower hole-doping for a given local gate voltage. This manifests quite directly as a shift of the efficiency peak vs gate voltage, though the peak amplitude is not substantially affected as the optimal carrier density is still achieved.

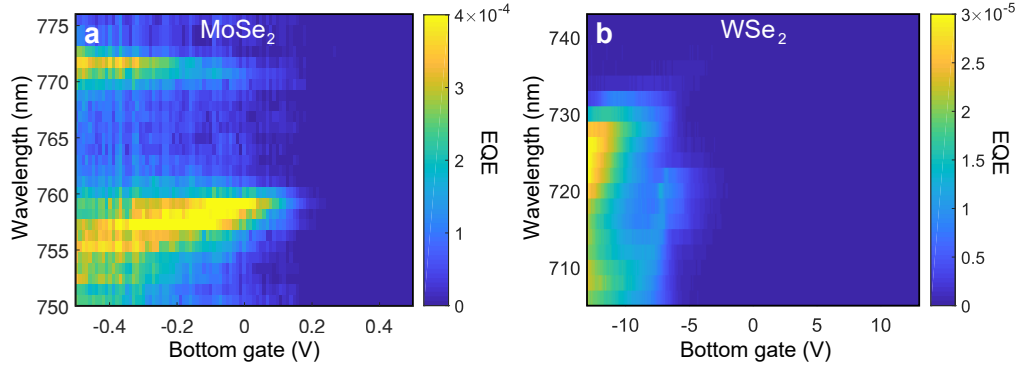


FIG. 11. | **Photocurrent efficiency under resonant excitation** Photocurrent EQE as a function of excitation wavelength and local gate voltage for MoSe₂ (a) and WSe₂ (b) showing that overall efficiency is still substantially lower for WSe₂, as expected from the difference in band alignment relative to neutral exciton energy.

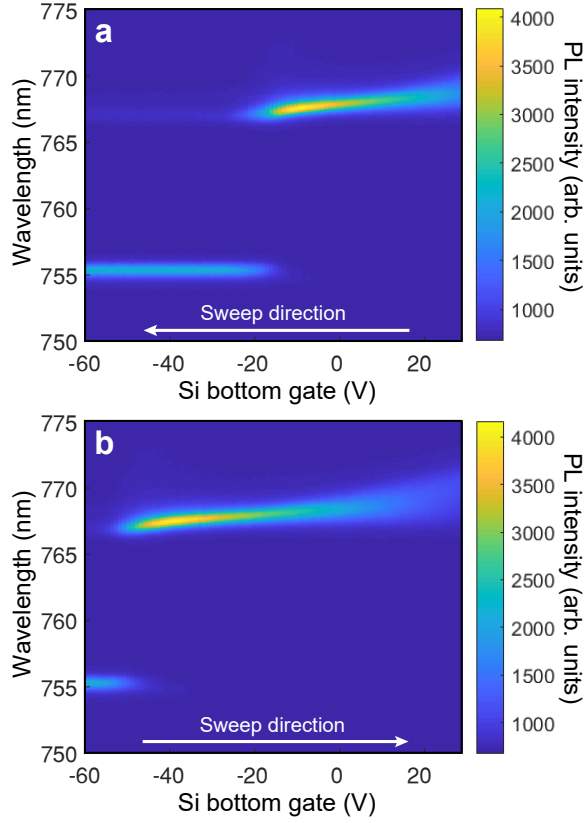


FIG. 12. | **Contactless charge injection and gate dragging** PL spectra under 660 nm excitation for an encapsulated MoSe₂ device separated from a Si bottom gate by a 285 nm oxide dielectric. Upon a downward sweep in gate voltage (**a**) the TMD passes through the undoped regime but is only able to weakly hole dope, with no changes to PL emission for arbitrarily negative gate voltage. When the sweep is subsequently reversed, however, a rapid transition to electron doping is seen. This behaviour is consistent with an accumulation of trapped charges at the hBN-oxide interface, built up by photoexcitation of holes during the downward sweep and locked in place due to the lack of direct electrical contact to charge traps at this interface between two insulators.

-
- [1] G. Kresse and J. Furthmüller, Physical review B **54**, 11169 (1996).
- [2] J. Heyd, G. E. Scuseria, and M. Ernzerhof, The Journal of chemical physics **118**, 8207 (2003).
- [3] S. Grimme, J. Antony, S. Ehrlich, and H. Krieg, The Journal of chemical physics **132**, 154104 (2010).